Composite Structures 252 (2020) 112665

Contents lists available at ScienceDirect

Composite Structures

journal homepage: www.elsevier.com/locate/compstruct

Failure simulation and design optimization of bioinspired heterogeneous interfaces by Floquet-based bar-spring model

Kun Geng [a], Wen Xie [a], Bin Chen [a], Qifang Yin [a], Yanan Yuan [a,*], Zuoqi Zhang [a,b,*]

[a] School of Civil Engineering, Wuhan University, Wuhan 430072, China
[b] Suzhou Institute of Wuhan University, Suzhou 215123, China

ARTICLE INFO

Keywords:
Interface optimization
Bioinspired design
Non-uniform pattern
Croslink

ABSTRACT

Interface plays a critical role in the mechanical performance of composites. Lack of a suitable interface design has long been a bottleneck impeding the full exploitation of the mechanical strengths of many superior reinforcement phases such as the high-performance carbon fibers and carbon nanotubes. Here a Floquet-based bar-spring model is developed to simulate the elastic and failure behaviors of three topological designs of heterogeneous interface inspired by the load-bearing biological materials in nature: end-concentrated, center-concentrated, and uniform pattern. Through comparative analyses, the advantages and disadvantages of every topological design are presented, and the guidelines of design optimization are summarized. The newly developed method is convenient and computationally economical for studying the mechanical behaviors of fiber/platelet reinforced composites. The study on the bioinspired design of interfaces not only shed lights on the interface strengthening and toughening mechanisms in natural materials but also give valuable guidelines for artificial interface designs.

1. Introduction

Interface plays a critical role in the mechanical performance of composites as well as other heterogeneous materials. Lack of a suitable interface design has long been a bottleneck impeding the full exploitation of the superior mechanical properties of many excellent reinforcement phases such as the high performance carbon fibers and the newly rising superstar candidates including carbon nanotubes, graphene and graphene oxide. Load-bearing biological composites in nature such as nacre, bone and collagen provide excellent examples of decent interface design greatly tuning material properties. In particular, nacre contains about 95% of stiff and brittle mineral platelets in volume fraction but achieves great integrative mechanical properties, specifically high stiffness (60–70 GPa), strength (140–170 MPa) and toughness (350–1240 J/m^2) [1–3]. It is quite amazing that the toughness of nacre is more than 3000 times higher than that of a monolithic aragonite platelet [4,5], since nacre almost has the same composition with the monolithic aragonite except its fabulous interfaces filled with a trivial quantity of biopolymers. This strongly suggests that the fine and complex interface design should play a crucial role in the strengthening and toughening mechanisms of nacre and similar load-bearing biological materials [6].

Fig. 1 schematically illustrates the typical microstructural organizations of platelet/fiber elements and finely structured interfaces in nacre shells and collagen fibers. Nacre shell has the well-known “brick-and-mortar” microstructure, in which the “bricks” referring to aragonite platelets are arranged in a staggered pattern in the “mortar” referring to organic matrices composed of protein and polysaccharide [2,7], as shown in Fig. 1a. In addition, the inter-platelet interface features with a large number of mineral bridges embedded in the thin layer of organic matrix, which is believed playing an important role in the strengthening and toughening mechanism of nacre as well as its mineralization process [8,9]. Fig. 1b shows the multi-level structure of tendon fibers, at the bottom level of which the collagen molecules are unidirectionally aligned in a staggered fashion and crosslinked with covalent and non-covalent bonds [10,11]. In order to investigate the structure–function relationship of these load-bearing biological materials, many research efforts have been made and much progress has been achieved in terms of theoretical modeling, computational simulation as well as experimental demonstration. A series of microscopic models such as tension-shear chain models [12–16], extended shear-lag models [17–19], suture mosaic model [20,21] have been developed to reveal how loadings are efficiently transferred between reinforcements via these interfaces and how the balanced and out-

* Corresponding authors at: School of Civil Engineering, Wuhan University, Wuhan 430072, China (Y. Yuan, Z. Zhang).
E-mail addresses: yuanyn@whu.edu.cn (Y. Yuan), zhang_zuoqi@whu.edu.cn (Z. Zhang).

https://doi.org/10.1016/j.compstruct.2020.112665
Received 3 January 2020; Revised 2 May 2020; Accepted 18 June 2020
Available online 29 June 2020

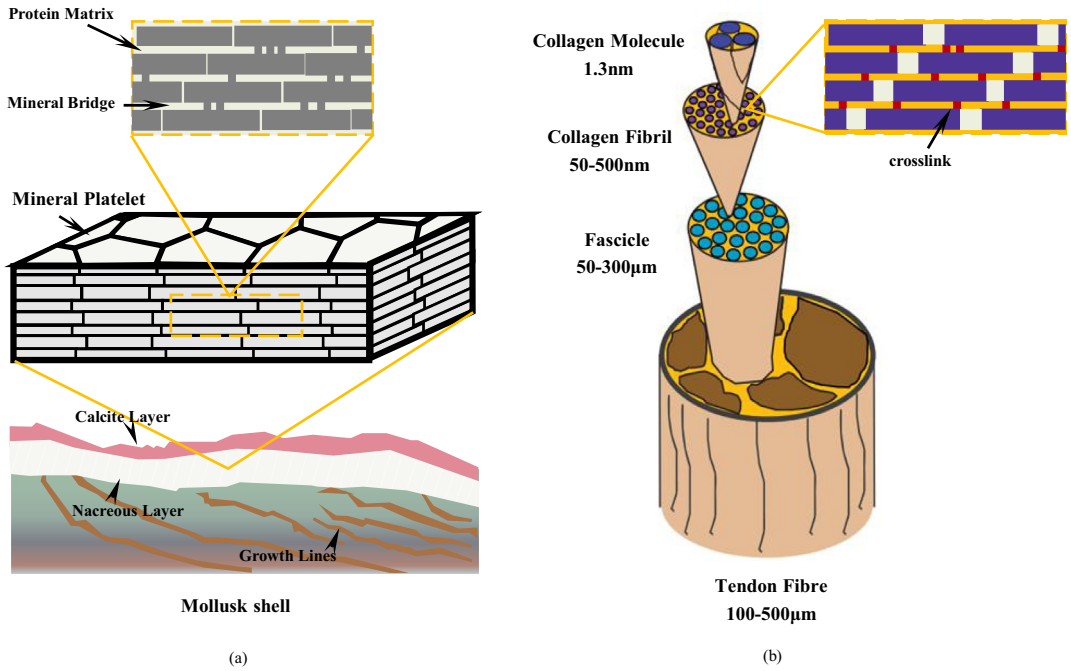

Fig. 1. Schematics of the crosslinked interfaces between neighboring mineral platelets in mollusk shell (a), and between neighboring tropocollagen molecules in mineralized tendon fibers (b).

standing integral mechanical properties are achieved through optimized selections of topological, geometrical and physical parameters. In particular, the interfaces can promote several strengthening and toughening mechanisms including shear fracture of mineral bridge, large visco-plastic deformation of biopolymer matrix, and frictional energy dissipation by sliding along uneven interfaces [22–24], when the nacre is gradually stretched to failure along the direction of aragonite wafer. Song et al. made a direct observations and statistical analyses of the mineral bridges embedded in the organic layers between aragonite platelets, and showed that their existence can significantly enhance the stiffness, strength and toughness of the organic layer, and proposed a "brick-bridge-mortar" arrangement instead of the traditional "brick–mortar" one to better describe the microarchitecture of nacre [25]. Meyers et al. studied the role of mineral bridges and soft organic layers in the mechanical strength of abalone nacre and declared that the primary role of the organic layer is to subdivide the monolithic aragonite into platelets of tens of nanometers thick and the mineral bridges with a density approximately 2.25/μm^2 are mainly responsible of the tensile strength perpendicular to the aragonite platelet [26]. Alghamdi et al. experimentally studied the facture behaviors of nacre under pure shear stress of torsion, and demonstrated that the mineral bridges made a dominant contribution to resist the initial tablet sliding [27,28]. Gu et al. 3D printed composite samples with "brick-bridge-mortar" microstructures and studied the effects of mineral volume fraction and mineral bridge number on the composite mechanical properties [29]. They suggested that solely increasing the number of mineral bridges would always add much benefit to the composite strength but not toughness. Niebel et al. manufactured nacre-like composites by infiltrating ceramic scaffolds with three drastically different polymers: a soft and weak elastomer, a strong, stiff and brittle thermoplastic, and a tough polymer of intermediate strength and stiffness, and showed that the crack initiation toughness correlates strongly with the polymer phases while the rising R-curve is mainly attributed to the mineral bridges and nano-asperities in the porous scaffold [30]. However, it is worth noting that only uniform or random distributions of mineral bridges are concerned in the existing studies, and decent investigations on the advantages and disadvantages of the variations on the distribution pattern, even though a great deal of evidences have clearly suggested that the mineral bridges in nacre are seen more in a central region of each platelet [25] while the covalent crosslinks in collagen are mainly located at the ends [10].

The biological interfaces and their induced amazing mechanical properties of biological composites have attracted material scientists and engineers to develop bioinspired designs for high performance synthetic materials [31–33]. A typical example is the development of bioinspired carbon nanotube fibers [34,35], in which several bioinspired interface designs were introduced to overcome the well-known weak interface bottleneck impeding the application of carbon nanotube fibers as a structural composite reinforcement. Our previous works proposed a collagen-mimic design of carbon nanotube bundles, studied the effect of crosslinked interfaces by an elastic model and atomistic simulations, and predicted that the crosslinks' introduction can greatly scale up the stiffness and strength of carbon nanotube bundles and the selection of crosslink density can efficiently tune their fracture modes and optimize their fracture toughness [35–37]. Park et al. introduced aromatic crosslinks between carbon nanotubes by aryl crosslinking reaction and the resulted carbon nanotube fibers exhibited superior specific Young's modulus and tensile strength to the strongest commercial carbon fibers [38]. In the design and fabrication of these bioinspired composites, much attention has been paid to the proper choice of crosslink type and density [39], but little has been done on the topological design of crosslink distribution, a selection and optimization of which may further improve the mechanical performances of these synthetic composites.

In order to reveal the underlying strengthening and toughening mechanism of the non-uniformly crosslinked interfaces inspired by natural biological materials and draw some principal guidelines for bioinspired interface design in synthetic composites, here a newly developed Floquet-based bar-spring model [40] is utilized to simulate the elastic and failure behaviors of three topological designs of crosslinked interfaces inspired by nature, namely, end-concentrated distribution, center-concentrated distribution and uniform distribution. Through comparative analyses, the advantages and disadvantages of each topological design are identified, and the guidelines for design

optimization are summarized. In particular, the remaining part of the paper is organized in the following structure. Section 2 introduces the bar-spring model and calculation procedure for failure simulations, and then Section 3 gives the results and analyses of calculations on the three bioinspired patterns of crosslinked interfaces. Finally, a summary is made in Section 4.

2. Problem description and modeling

A variety of non-uniformly crosslinked interfaces are widely seen in load-bearing biological materials in nature, and it raises a fundamental scientific question: what are the advantages and disadvantages of these non-uniform interfaces, especially in terms of their roles in stiffening, strengthening and toughening mechanism. To answer this question, we classify the non-uniform interfaces into three major topological patterns, namely end-concentrated distribution, center-concentrated distribution and uniform distribution, represented by three simplified basic unit models shown in Fig. 2a. The dark (blue in colored version) part represents the stiff reinforcements while the light (yellow in colored version) part represents the relatively soft matrix. It is worth noting that the matrix here can be real continuum materials or virtual materials equivalent to the interactions among reinforcements. Comparative studies are conducted among the three representative patterns with our newly developed Floquet-based bar-spring model to demonstrate their respective mechanical advantages and disadvantages under different physical and geometrical conditions. The Floquet-based bar-spring model is built on the foundation of Floquet theory [40] and provides a computationally economical and generic approach for generalized staggered composites even with heterogeneous and non-uniform reinforcements aligned in an arbitrary staggered fashion in heterogeneous matrix. In the current paper, the Floquet-based bar-spring model is further developed to not only evaluate the elastic mechanical properties of arbitrary staggered composites but also simulate the detailed failure behaviors in the composites. The Floquet-based bar-spring model for the non-uniform interfaces is shown in Fig. 2b, in which the stiff reinforcements are converted to bars and the soft matrix to a series of heterogeneous shear springs. The basic unit is divided into N segments according to the variation of bar tensile stiffness and distributed shear spring constant so that all the tensile stiffness of each bar (k_i^q) and the shear spring constant of each shear spring domain (k_{ij}^q) are constant in the arbitrary qth segment, where $i, j = 1, 2$ denote the bar sequence, and $q = 1,\ldots, N$ the segment sequence. Let the total length of the unit be L, and the length of the qth segment be l_q. The segmentation and effective mechanical parameters (k_i^q, k_{ij}^q, and etc) can be freely defined according to the heterogeneous system of interest. Fig. 2c shows an infinitesimal element of the ith bar in the qth segment, subjected to the axial forces $t_i(x)$ with corresponding displacement $u_i(x)$ and the shear stress $\tau_{ij}(x)$ prescribed by the jth bar through the distributed shear springs between them. The coordinate x is originated at the fixed left end and pointed to the right. Analysis on the equilibrium and deformation of the infinitesimal element leads to

$$\tau_{ij} = k_{ij}^q(u_j - u_i) \tag{1}$$

$$\frac{\mathrm{d}t_i}{\mathrm{d}x} = -\sum_{j=1,j\neq i}^{2} k_{ij}^q(u_j - u_i) \tag{2}$$

$$\frac{\mathrm{d}u_i}{\mathrm{d}x} = \frac{t_i}{k_i^q} \tag{3}$$

where $i = 1,2$, $q = 1,\ldots, N$. Introducing a column vector $\boldsymbol{\xi} = (t_1, u_1, t_2, u_2)^{\mathrm{T}}$, the system of equations can be reformatted in the form of matrices as follows

$$\frac{\mathrm{d}\xi}{\mathrm{d}x} = \mathbf{A}_q\boldsymbol{\xi} \tag{4}$$

where $\mathbf{A}_q$ is a 4-order constant matrix

$$\mathbf{A}_q = \begin{bmatrix} 0 & k_{12}^q & 0 & -k_{12}^q \\ \frac{1}{k_1^q} & 0 & 0 & 0 \\ 0 & -k_{21}^q & 0 & k_{21}^q \\ 0 & 0 & \frac{1}{k_2^q} & 0 \end{bmatrix} \tag{5}$$

where $q = 1, 2, \cdots, N$. The governing equations indicate that the system is a typical Floquet system, and thus the model is named to be the Floquet-based bar-spring model [40].

The qth segment begins at $x_{q-1} = \sum_{i=1}^{q-1} l_i$ and ends at $x_q = \sum_{i=1}^{q} l_i$, i.e., $x \in [x_{q-1},\ x_q]$. Making a Taylor's expansion of $\boldsymbol{\xi}(x)$ of the qth segment at its beginning point x_{q-1}, we obtain

$$\boldsymbol{\xi}(x) = \boldsymbol{\xi}(x_{q-1}) + (x - x_{q-1})\boldsymbol{\xi}' + \frac{1}{2!}(x - x_{q-1})^2\boldsymbol{\xi}''(x_{q-1}) + \ldots \tag{6}$$

According to the derivative operation of matrix function, we can get

$$\boldsymbol{\xi}'(x_{q-1}) = \frac{d\xi}{dx} = \mathbf{A}_q\boldsymbol{\xi}(x_{q-1}),\ \boldsymbol{\xi}''(x_{q-1}) = \frac{d^2\xi}{dx^2} = \mathbf{A}_q^2\boldsymbol{\xi}(x_{q-1}),\ \ldots \tag{7}$$

Substitute the above equation into Eq. (5), we have

$$\begin{aligned} \boldsymbol{\xi}(x) &= \boldsymbol{\xi}(x_{q-1}) + (x - x_{q-1})\mathbf{A}_q\boldsymbol{\xi}(x_{q-1}) + \tfrac{1}{2!}(x - x_{q-1})^2\mathbf{A}_q^2\boldsymbol{\xi}(x_{q-1}) + \ldots \\ &= \left[\mathbf{I} + (x - x_{q-1})\mathbf{A}_q + \tfrac{1}{2!}(x - x_{q-1})^2\mathbf{A}_q^2 + \ldots\right]\boldsymbol{\xi}(x_{q-1}) \\ &= e^{\mathbf{A}_q(x - l_{q-1})}\boldsymbol{\xi}(x_{q-1}) \end{aligned} \tag{8}$$

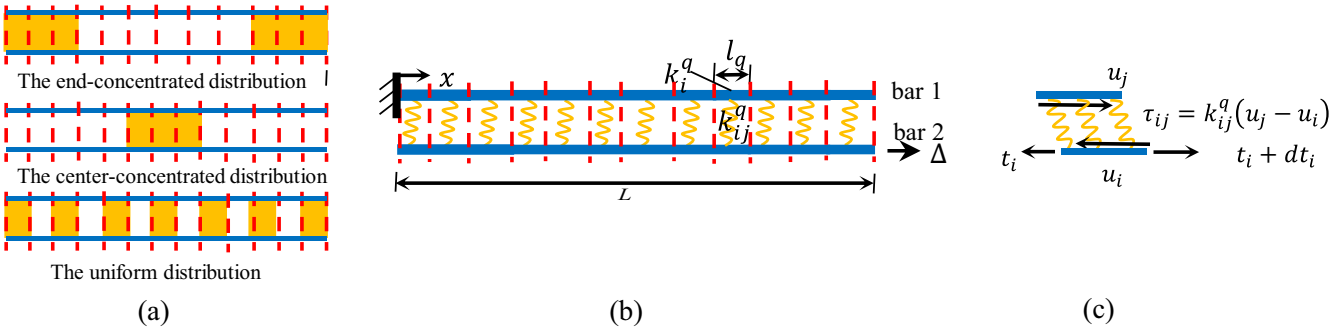

Fig. 2. (a) Three typical pattern of interface design inspired from the load-bearing biological materials in nature: the end-concentrated distribution, the center-concentrated distribution, and the uniform distribution; (b) a general Floquet-based bar-spring model for studying the non-uniform interfaces; (c) the equilibrium analysis on an infinitesimal element of bar.

in which $x \in [x_{q-1},\ x_q]$. Therefore, the following result can be immediately derived

$$\boldsymbol{\xi}(x_q) = e^{\mathbf{A}_q l_q}\boldsymbol{\xi}(x_{q-1}) \tag{9}$$

Apply Eq. (8) recursively as q varies from 1 to N, and get

$$\boldsymbol{\xi}(L) = e^{l_N \mathbf{A}_N} \ldots e^{l_2 \mathbf{A}_2} e^{l_1 \mathbf{A}_1}\boldsymbol{\xi}(0) \tag{10}$$

Adopting the matrix format, the linear equations above can be rewritten to be

$$\begin{bmatrix} t_1(L) \\ u_1(L) \\ t_2(L) \\ u_2(L) \end{bmatrix} = \prod_{q=1}^{N} (\nabla) e^{\mathbf{A}_q l_q} \begin{bmatrix} t_1(0) \\ u_1(0) \\ t_2(0) \\ u_2(0) \end{bmatrix} \tag{11}$$

in which (∇) indicates the product is ordered with respect to decreasing q. For the unit cell under displacement loading Δ as shown in Fig. 2b, the boundary conditions are

$$\left.\begin{array}{l} u_1(0) = 0 \\ t_2(0) = 0 \\ t_1(L) = 0 \\ u_2(L) = \Delta \end{array}\right\} \tag{12}$$

As the characteristic matrices A_q and segment length l_q are all known, the four unknown boundary values can be solved from the four independent linear equations in Eq. (11). As the eight boundary values of axial force and displacement are known, the average strain and stress of the structure can be, respectively, calculated by

$$\bar{\varepsilon} = \frac{\Delta}{L} \tag{13}$$

$$\bar{\sigma} = \sum_{i=1}^{M} t_i(L)/S \tag{14}$$

in which S is the cross-sectional area of the structure, i.e., the lateral dimension in the 2-dimensional cases. Therefore, the effective Young's modulus of the structure can be evaluated by

$$E_{eff} = \bar{\sigma} / \bar{\varepsilon} \tag{15}$$

Regarding the application of the Floquet-based bar-spring model to calculate the effective Young's modulus of the bioinspired composites with arbitrary staggered structures, one is referred to our previous work Ref. [40].

As soon as $\boldsymbol{\xi}(0)$ is obtained, Eqs. (8) and (9) can be utilized in a recursive way to give the piecewise solution of $\boldsymbol{\xi}(x)$, i.e., $t_i(x)$ and $u_i(x)$. Furthermore, Eq. (1) can provide the shear stress function along the interface $\tau_{ij}(x)$. With these functions known, assume both the reinforcement and matrix material are linear elastic up to brittle failure, and the failure occurrence in the bar or interface segments can be determined by the following criterion

$$\max\left\{\frac{\max t_i^q}{t_i^{fq}}, \frac{\max \tau_{ij}^q}{\tau_{ij}^{fq}}\right\} \geqslant 1 \tag{16}$$

in which t_i^{fq} and τ_{ij}^{fq} are the critical failure strength of bar and spring in the qth segment, respectively. The corresponding failure strain and strength of the structure at the moment can be calculated by

$$\bar{\varepsilon}^f = \Delta^f / L \tag{17}$$

$$\bar{\sigma}^f = \sum_{i=1}^{M} t_i^f(L)/S \tag{18}$$

where the superscript f indicates the quantities being taken at the failure moment. Remove the broken segment, update the corresponding characteristic matrix, continue increasing loadings on the remaining structure, and repeat the above procedure of calculation up to the complete failure of structure, we finally can get the whole curve of failure strength versus failure strain.

To better evaluate the interface performance, we'd better introduce the interface shear modulus, failure shear strength and strain. The total extension of the structure can be decomposed into two parts: one is the stretch of the bars and the other is originated from the shear deformation of interface layer. It can be inferred with ease that the part of displacement due to interface shear deformation can be presented by $u_2(0)$ in Fig. 2b. Hence, the average shear strain can be calculated by

$$\bar{\gamma} = u_2(0)/b \tag{19}$$

The average shear stress along the interface is

$$\bar{\tau} = t_2(L)/L \tag{20}$$

Then, we can get the effective shear modulus of the interface

$$\bar{G} = \bar{\tau} / \bar{\gamma} \tag{21}$$

Denoting the displacement $u_2(0)$ and axial force $t_2(L)$ at the failure moment by $u_2^f(0)$ and $t_2^f(L)$, respectively, the failure shear strain and strength of the interface can be calculated by

$$\bar{\gamma}^f = u_2^f(0)/b \tag{22}$$

$$\bar{\tau}^f = t_2^f(L)/L \tag{23}$$

According to the description above, the calculation procedure is summarized in Fig. 3. We can see that the Floquet-based bar-spring model is able to simulate the failure process of the composite structure and give out the complete curves of the stress against strain. Consequently, the effective stiffness, failure stress, strain and toughness of the interface as well those of the structure can be obtained. Since the current paper mainly concerns the interface design, we will just focus on the mechanical performance and failure behaviors of interfaces in the remaining of the paper and assume that the reinforcements are homogeneous and linear elastic without premature failures. However, it is worth noting that the Floquet-based bar-spring model and calculation procedure established above can also study the failure behaviors and relevant mechanical properties of unidirectionally reinforced composites with more general and complex microstructures.

3. Results and discussion

As mentioned in the introduction section, it is well known that weak interface has long been a bottleneck impeding the development of high performance carbon nanotube fibers and some novel interface designs are highly desired in the field. Thus, in this section a basic unit of the collagen-mimetic carbon nanotube bundles in Fig. 4a was taken as an example to comparatively demonstrate the advantages and disadvantages of three typical heterogeneous interface designs. In the basic unit, two single-walled carbon nanotubes of chirality (6, 6) are crosslinked with a series of C–C covalent bonds. The atomic spacing along the interface is $d = 0.24$nm, and the largest crosslink number allowed is $N_{IF} = L/d$ when all the interface atoms are crosslinked. The number of crosslinks actually formed is dented by N_{CL}. The overall crosslink density is defined as the ratio $\rho = N_{CL}/N_{IF}$. To better capture the occurrence of each crosslink failure, the unit is segmented in such a way that each segment just contain one crosslink at most (see the example in Fig. 4a with $\rho = 100\%$). Correspondingly, the geometrical and physical parameters in the bar-spring models are listed as below

$b = 0.16$ nm

$l_q = d = 0.24$nm

$k_i^q = k = 809.375\,\mathrm{eV/\AA}$

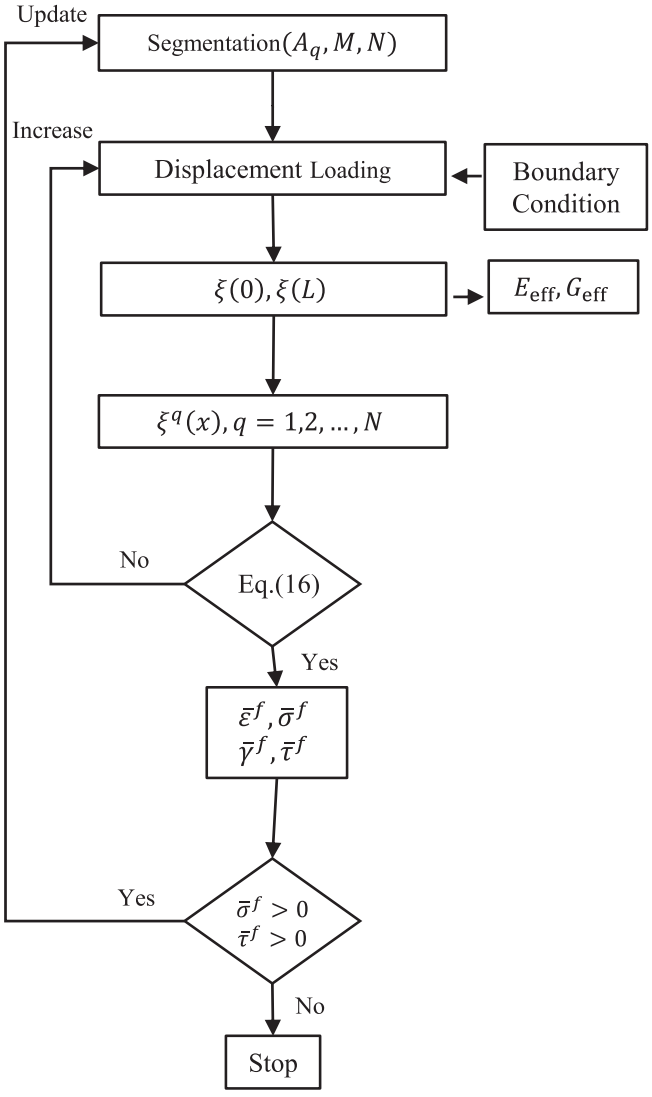

Fig. 3. The procedure for simulating the failure process of the composite structure and giving out the complete curves of the stress against strain according to the Floquet-based bar-spring model.

$$k_{ij}^q = \begin{cases} 1088\ \text{GPa} & \textit{if}\ \text{crossink exists} \\ 0 & \textit{otherwise} \end{cases}$$

$$\tau_{ij}^{fq} = \tau^f = 2.28835\,\text{eV/Å}^2$$

The mechanical parameters above are derived from the results of molecular dynamics simulations by Lin et al. [36]. To verify the newly developed Floquet-based bar-spring method, its simulation results for the uniform interface design with the crosslink density ρ = 48% and the interface length L = 8 nm are compared with those of the molecular dynamic simulations. The effective interface shear modulus, strength and failure initiation strain given by the Floquet-based bar-spring model are 1.64 eV/Å^2, 0.39 eV/Å^2 and 0.24, respectively, in good agreement with 1.57 eV/Å^2, 0.38 eV/Å^2 and 0.24 by the molecular dynamic simulation.

To gain a first sight on the load-transfer difference of the three typical interface designs, let us check their shear stress distributions along the interface as presented in Fig. 4b. In this example, the interface length L is taken to be 8 nm, the overall crosslink density $\rho = 48\%$ for all the three interfaces, and the prescribed displacement is very small to guarantee no crosslink failed at the moment. The shear stresses are normalized by their respective maximum values for the three interfaces to better show their shear stress distributions. We can see that for all the three distribution patterns the shear stress gets maximum at the outmost crosslinks and then gradually goes down to the central crosslinks. In the uniform distribution pattern the shear stress goes down quickly from the ends to the center. This is just as well as expected and quite understandable by the shear-lag theory [37]. The variation of shear stress in the center-concentrated distribution is essentially analogous to that of the uniform distribution except that the non-zero shear stress spreads over the smaller central crosslinked region. Due to the shorter interaction length and higher local crosslinked density, the shear stress in the center-concentrated pattern is more uniform than that of the uniform distribution pattern, which can be rationalized by the shear-lag theory as well. For the end-concentrated pattern, the shear stress all over the crosslinked regions maintains a relatively high level. To some extent, the end-concentrated distribution pattern can be regarded as the result by moving the crosslinks in the underloaded central region of the uniform distribution pattern to the overloaded end regions, and thus all the crosslinks can contribute more uniformly and efficiently. To quantitatively measure the utilization efficacy of the crosslinks, the ratio of effective working crosslinks can be defined as the ratio of the length of crosslinked region with stress level above a critical fraction of the maximum shear stress divided by the total length of crosslinked region. For example, if the critical fraction is set to be 10%, the ratio of effective working crosslinks are 75%, 100%, and 100%, respectively, for the uniform, center-concentrated, and end-concentrated pattern. In another word, there are 25% of the crosslinks almost bearing no load at all in the uniform distribution pattern. It is evident that the end-concentrated and center-concentrated interface designs can yield a higher efficacy of crosslink utilization. Interestingly, the curve of the end-concentrated pattern can be regarded as the result of breaking the center-concentrated curve into two parts from its middle point and moving them apart. In another word, the varying trends of shear stress for the two patterns are intrinsically the same, since their characteristic matrices are actually the same.

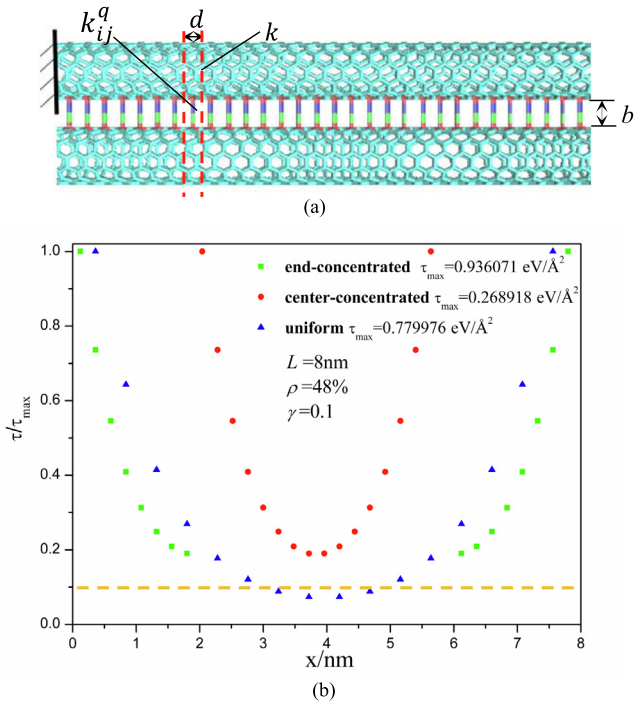

Fig. 4. (a) A crosslinked pair of carbon nanotubes adopted for demonstrating the interface design optimization, and (b) the variation of the shear stress along the interface for the three distribution patterns of crosslinks.

Fig. 5 shows the typical effective shear stress–strain curves of the three crosslinked interfaces, in which an interface length of 8 nm and a crosslink density of 48% are taken for example. All the curves are linear up to the onset of crosslink failure, and then oscillate several times, and finally drop to the state of complete interface failure. The oscillations between the initiation and completion of interface failure result from the fact that the interfaces considered here are composed of discrete crosslinks and each dip of the effective shear stress corresponds to a burst of crosslink break (see Fig. 6). It is worth noting that peak shear stresses are almost steady during the failure propagation for each interface design. Considering the shear stress distribution in Fig. 4b, the unchanged peak stress should be due to that some underloaded crosslinks turn to contribute more as soon as some overloaded crosslinks break and stop bearing stress. Comparisons among the three curves clearly show that the effective interface stiffness decreases from the end-concentrated pattern, to the uniform pattern, and the center-concentrated pattern in sequence. In contrast, the effective interface failure strain has a reverse trend. The end-concentrated and center-concentrated patterns are similar in the effective interface strength, and significantly superior to the uniform pattern.

Fig. 6 shows the typical process of failure propagation of the three crosslinked interfaces as the effective interface shear strain increases, in which all the interfaces have the same length 8 nm and crosslink density 48%. It can be seen that regardless of the distribution pattern the failure always initiates at the outmost crosslinks and then gradually propagates to the central ones. The failure sequence of crosslinks is in accordance with their stress level presented in Fig. 4b. As the effective shear stress goes up, the interface failure starts earliest and finish earliest in the end-concentrated pattern, while starts latest and finish latest in the center-concentrated pattern. The failure initiation and completion uniform pattern just falls in between the end- and center-concentrated patterns. This is consistent with the characteristic features of the effective shear stress versus strain curves in Fig. 5. Combining Figs. 5 and 6, the following principles can be concluded: (1) the crosslinks concentrated in a smaller region lead to more uniform shear stress distribution and simultaneous break, and consequently higher effective interface shear strength; (2) the more crosslinks are concentrated to the ends, the higher interface shear stiffness is obtained, and vice versa. Note that the modes of interface failure shown in Fig. 6 are highly symmetric, because the structures are completely symmetric. If the asymmetric structures are considered, the interface failures would not exhibit such a high degree of symmetry.

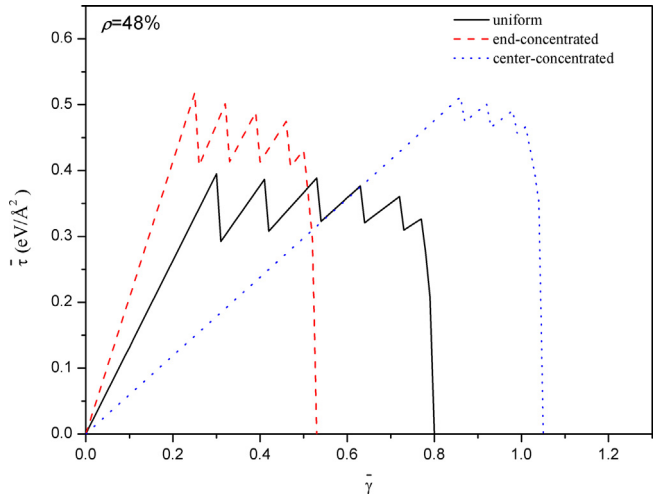

Fig. 5. The effective shear stress-shear strain curves of the three crosslinked interfaces. Here the interface length 8 nm and the crosslink density is 48%.

To make a quantitative comparison of the three interfaces in their mechanical properties, the mechanical parameters, namely the effective shear modulus, strength, failure strain and work of fracture are defined based on the shear stress–strain curves as shown in Fig. 5. The effective shear modulus as defined in Eq. (21) can also be regarded as the inclination of the initial linear segment of the curves. The effective shear strength and failure strain, respectively, defined in Eqs. (22) and (23), are dependent on the interface failure status. For simplicity, hereafter we adopt their respective maximum values as the effective shear strength and failure strain, corresponding to the peak shear stress at the initiation of crosslink failure and the ultimate strain at the end of interface failure in the stress–strain curve, respectively. Fig. 7 show the comparison of the three interface designs in the mechanical parameters for a variety of crosslink densities. It can be seen that the center-concentrated pattern is superior in the effective interface strength, failure strain and work of fracture but inferior in the effective interface shear modulus, while the end-concentrated pattern is superior in the effective interface shear modulus and strength but inferior in the effective failure strain and work of fracture. However, both of them seem superior to the uniform pattern of design in the overall mechanical performances. This may well rationalize the aforementioned observations that the distributions of mineral bridges in nacre shells and covalent crosslinks in collagen fibrils are either center-concentrated or end-concentrated. Note that the effective interface strength of the end-concentrated is slightly but unusually low at the very small crosslink density of 9%, which is because there are only 1 or 2 crosslinks at each end and the premature failure of the interface at either end is inclined to happen in the failure simulation.

Limit our attention to the failure properties at initiation, and the fine segmentation shown in Fig. 4a, which is mainly for the convenience of segment adaptation during the crosslink failure propagation, will become unnecessary. Therefore, as shown in Fig. 8 we can homogenize the crosslinked regions of interface with an effective shear spring constant, and characterize the end-concentrated, center-concentrated, and uniform interface with the three-, three- and single-segment Floquet-based bar-spring model, respectively. The segmentations are according to the division of crosslinked and non-crosslinked regions. In the crosslinked regions, the effective shear spring constant and critical shear strength are, respectively, converted to be

$$k_{ij}^{q}=\begin{cases}\eta\cdot 1088\text{GPa} & \textit{if crossink exists}\\ 0 & \textit{otherwise}\end{cases}$$

$$\tau_{ij}^{fq}=\tau^{f}=\eta\cdot 2.28835\text{eV}/\text{Å}^{2},$$

$$\eta=\begin{cases}\rho & \text{for the uniform pattern}\\ 1 & \text{for the end - /center - concentrated pattern}\end{cases}$$

Here the coefficient r_i can be regarded as the local crosslink density defined over each crosslinked region. However, the local and global crosslink density is the same for the uniform pattern. With the simplistic models and converted physical parameters, following the procedure in Fig. 3 up to the interface failure initiation, we can obtain the analytical formulae of the effective shear modulus, shear strength, and failure initiation shear strain as functions of a variety of geometrical and physical parameters for the three typical interface designs. Introducing three dimensionless parameters $\lambda=b\sqrt{2k_{ij}^{q}/k}$, $\zeta=d/b$ and $\beta=L/b$, the specific formulae are shown as below:

(1) the end-concentrated distribution

$$\bar{G}=\frac{\lambda k[\lambda\beta(1-\rho)(e^{2\lambda\beta\rho}-2e^{\lambda\beta\rho}+1)+2(e^{2\lambda\beta\rho}-1)]}{b\beta[\lambda\beta(1-\rho)(e^{2\lambda\beta\rho}-1)+2(e^{2\lambda\beta\rho}+2e^{\lambda\beta\rho}+1)]} \tag{24}$$

$$\bar{\tau}^{f}=\frac{2\zeta\tau^{f}[\lambda\beta(1-\rho)(e^{2\lambda\beta\rho}-2e^{\lambda\beta\rho}+1)+2(e^{2\lambda\beta\rho}-1)]}{\beta[\lambda\beta(1-\rho)(e^{2\lambda\beta\rho}-2e^{\lambda\beta\rho}+1)+2(e^{2\lambda\beta\rho}-1)-\Theta]} \tag{25}$$

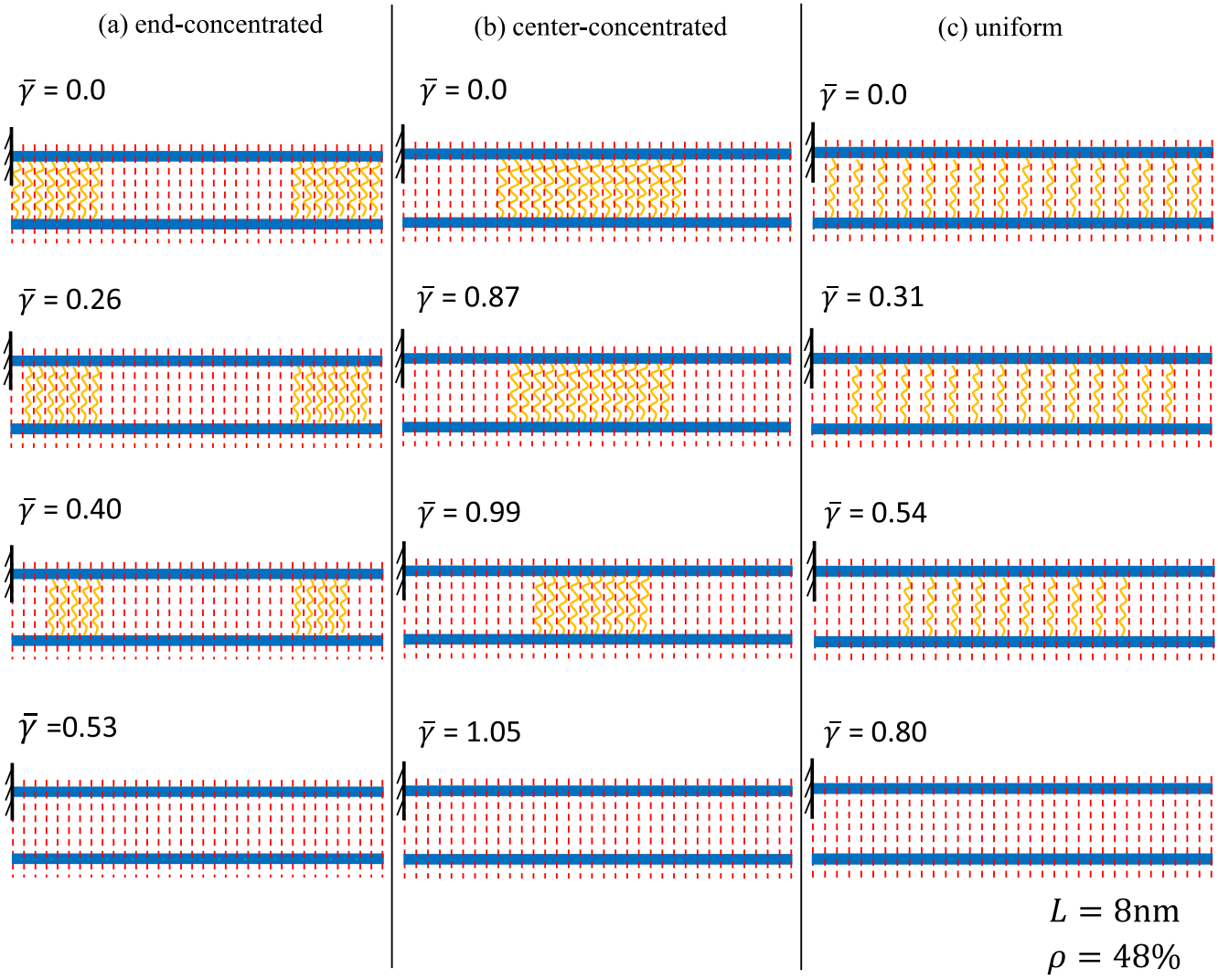

Fig. 6. Failure propagation of the three crosslinked interfaces. Here the interface length 8 nm and the crosslink density is 48%.

$$\bar{\gamma}_I^f = \frac{2\zeta b\tau^f[2(e^{2\lambda\beta\rho}+2e^{\lambda\beta\rho}+1)+\lambda\beta(1-\rho)(e^{2\lambda\beta\rho}-1)]}{\lambda k[\lambda\beta(1-\rho)(e^{2\lambda\beta\rho}-2e^{\lambda\beta\rho}+1)+2(e^{2\lambda\beta\rho}-1)-\Theta]} \tag{26}$$

where

$$\Theta = \lambda\beta(1-\rho)\left(e^{\lambda(2\beta\rho-\zeta)}-e^{\lambda(\beta\rho-\zeta)}-e^{\lambda(\beta\rho+\zeta)}+e^{\lambda\zeta}\right) + 2\left(e^{\lambda(2\beta\rho-\zeta)}+e^{\lambda(\beta\rho-\zeta)}-e^{\lambda(\beta\rho+\zeta)}-e^{\lambda\zeta}\right)$$

(2) the center-concentrated distribution

$$\bar{G} = \frac{2\lambda k(e^{\lambda\beta\rho}-1)}{b\beta[(2+\lambda\beta-\lambda\beta\rho)e^{\lambda\beta\rho}+2-\lambda\beta+\lambda\beta\rho]} \tag{27}$$

$$\bar{\tau}^f = \frac{2\zeta\tau^f(e^{\lambda\beta\rho}-1)}{\beta(e^{\lambda\beta\rho}-e^{\lambda(\beta\rho-\zeta)}+e^{\lambda\zeta}-1)} \tag{28}$$

$$\bar{\gamma}_I^f = \frac{\zeta b\tau^f[(2+\lambda\beta-\lambda\beta\rho)e^{\lambda\beta\rho}+2-\lambda\beta+\lambda\beta\rho]}{\lambda k(e^{\lambda\beta\rho}-e^{\lambda(\beta\rho-\zeta)}+e^{\lambda\zeta}-1)} \tag{29}$$

(3) the uniform distribution

$$\bar{G} = \frac{\lambda k\sqrt{\rho}(e^{\lambda\beta\sqrt{\rho}}-1)}{b\beta(e^{\lambda\beta\sqrt{\rho}}+1)} \tag{30}$$

$$\bar{\tau}^f = \frac{2\rho\zeta\tau^f(e^{\lambda\beta\sqrt{\rho}}-1)}{\beta(e^{\lambda\beta\sqrt{\rho}}-e^{\lambda(\beta-\zeta)\sqrt{\rho}}+e^{\lambda\zeta\sqrt{\rho}}-1)} \tag{31}$$

$$\bar{\gamma}_I^f = \frac{2\sqrt{\rho}\zeta b\tau^f(e^{\lambda\beta\sqrt{\rho}}+1)}{\lambda k(e^{\lambda\beta\sqrt{\rho}}-e^{\lambda(\beta-\zeta)\sqrt{\rho}}+e^{\lambda\zeta\sqrt{\rho}}-1)} \tag{32}$$

With these formulae above, all the curves of the interface properties varying with the interface length and crosslink density can be plotted for the three interface designs, see Fig. 9 with the simulation results (data points) from the aforementioned fine segmented Floquet-based bar-spring models included for comparison purposes. In Fig. 9, the column number (1), (2), and (3) refer to the end-concentrated, center-concentrated, and uniform interface design, respectively, while the row number (a), (b), and (c) represent the effective interface shear modulus, shear strength, and failure initiation strain, respectively. Overall, the newly developed analytical results agree well with the aforementioned simulation results, suggesting that the analytical formulae provide a convenient and quick way to deliver reasonable predictions for the interface design and optimization. It is worth noting that there can be seen a little large discrepancy between the analytical and simulation results in the facture initiation shear strain of the end-concentrated interface design when the crosslink density $\rho = 9\%$ and the interface length $L = 8$ nm. This is because that in

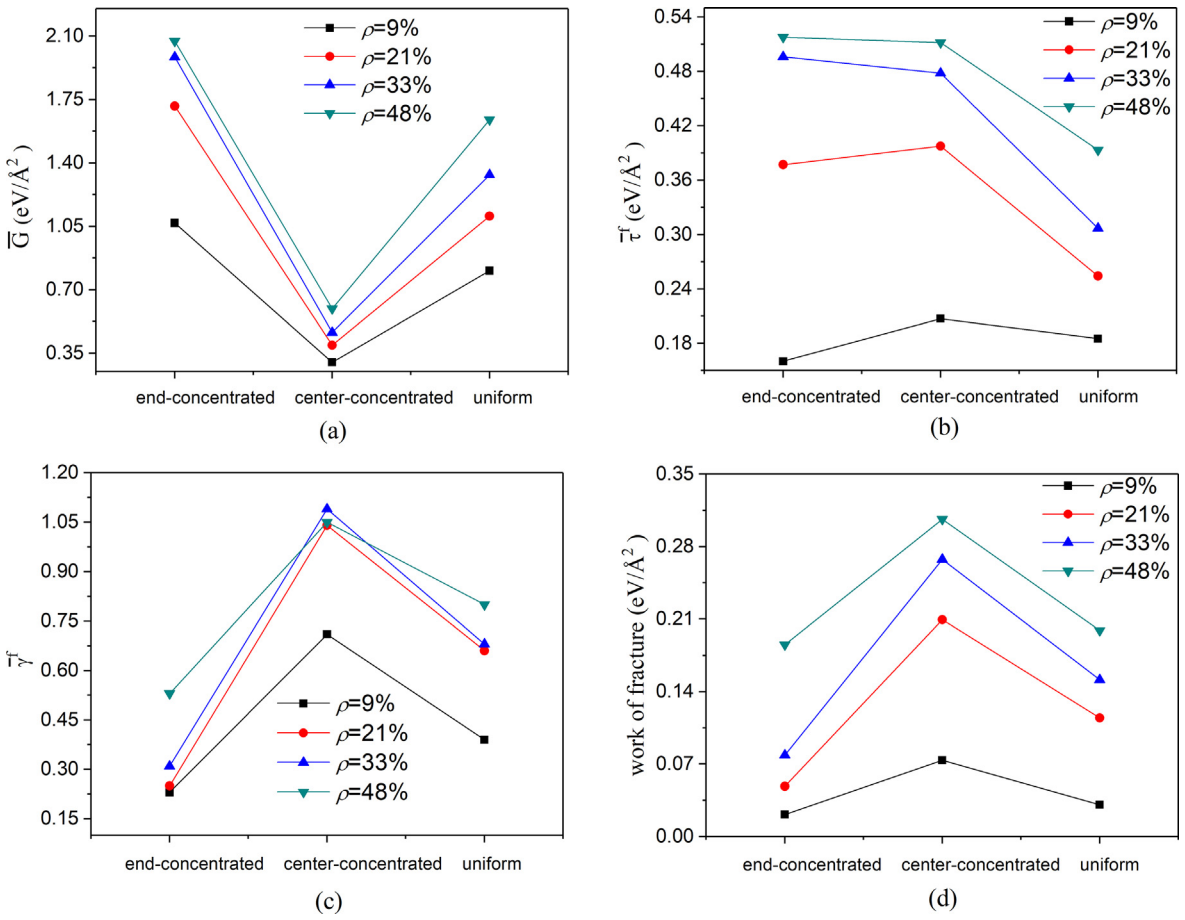

Fig. 7. Interface property comparison among the three distributions of crosslinks: (a) Effective shear modulus, (b) shear strength, (c) failure shear strain, and (d) work of facture. Here the interface length is taken to be 8 nm.

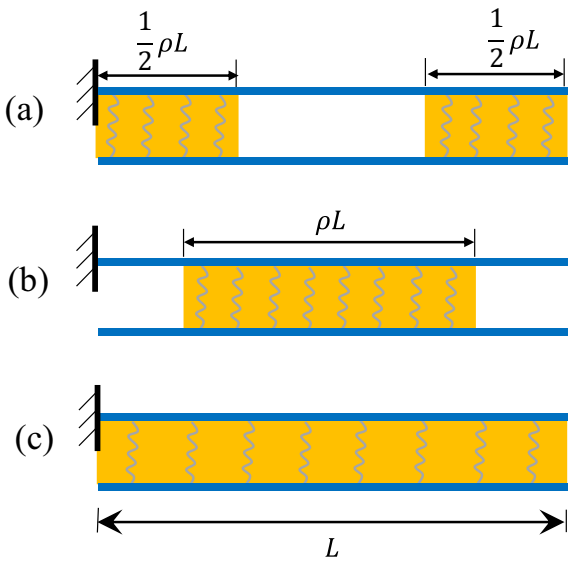

Fig. 8. The simplistic Floquet-based bar-spring models focused on the elastic behavior and failure initiation of interfaces: (a) the end-concentrated, (b) center-concentrated, and (c) uniform interface. The segmentations are according to the division of crosslinked and non-crosslinked regions.

this case there are only 3 crosslinks and they cannot be symmetrically distributed at the two ends in the fine segmented model, but the simplistic analytical model homogenizes the crosslinks and still ideally symmetric. However, the difference becomes trivial as soon as the crosslink number increases. For all the three designs, it can be inferred from Fig. 9a1-3 that increasing the crosslink density is always increasing the effective shear modulus while increasing the interface length is always reducing the effective shear modulus. When the interface length is long, the effect of crosslink density is less pronounced. With respect to the effective interface shear strength, similar trends can be concluded from Fig. 9b1-3. The varying trend should be attributed to the non-uniform distribution of shear stress along the interfaces, i.e., the ratio of effective working crosslinks significantly decreases as the interface length increases. It is also worth mentioning that for the uniform interface design the varying trends of the effective interface shear modulus and strength predicted by the Floquet-based bar-spring model are in good consistency with our previous results by molecular dynamic simulations [36]. Coming to the effective failure initiation shear strain shown in Fig. 9c1-3, for the end-concentrated and uniform designs one can see that the effective failure initiation shear strain only slightly varies with both the crosslink density and interface length around the effective failure shear strain of a single crosslink. This is just as expected since the interface failure initiation always occurs at the crosslink at one end as shown in Fig. 6. For the center-concentrated design, the effective failure initiation shear strain is always increasing with the increase of either crosslink density or interface length, because in this case it contains a part of the CNT elongation which is always increasing with crosslink density and interface length. From the above analysis, we can find that the crosslinking density, distribution, and interface length all have important effects on the mechanical properties of the crosslinked interfaces and in turn the mechanical properties of the bioinspired carbon nanotube bundles.

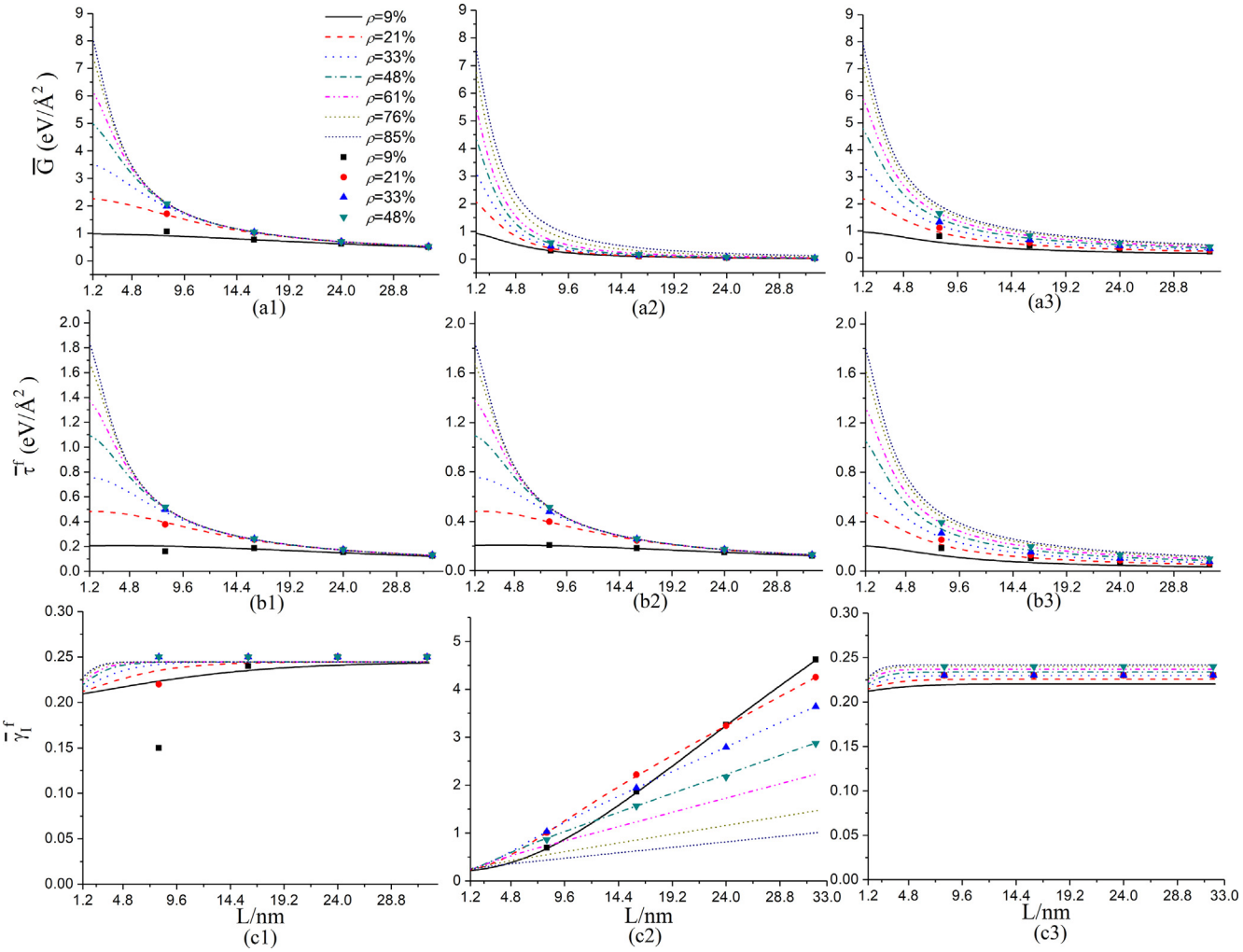

Fig. 9. The variation of effective interface properties with respect to interface length and crosslink density for the three distribution modes: the column number (1), (2), and (3) refer to the end-concentrated, center-concentrated, and uniform pattern, respectively, while the row number (a), (b), and (c) represent the effective interface shear modulus, shear strength, and failure initiation strain, respectively. Note that the smooth curves are given by the analytical functions while the data points are from the simulations of fine segmented Floquet-based bar-spring model.

The analytical formulae above provide a convenient and economic methods to predict the mechanical properties of different interface designs as well as to figure out the optimal design through tuning a range of geometrical and physical parameters.

Even though the crosslinked interface of carbon nanotube bundles is chosen as a demonstration system in this section, the model and analyses presented here can be easily extended to a variety of interfaces in natural and synthetic composites. Especially, it should be emphasized that the principal trends and mechanisms unveiled here are generic, independent of any specific demonstration systems utilized.

4. Summary

In the paper, a Floquet-based bar-spring model is developed to simulate the elastic and failure behaviors of three topological designs of crosslinked interface inspired by nature: end-concentrated, center-concentrated and uniformly distributed crosslinks. The newly developed model and simulation procedure provide a convenient and economic tool for studying the mechanical behaviors of a diversity of interfaces. The study on the bioinspired design of interfaces not only provide valuable guidelines for bioinspired interface designs but also shed lights on the interface stiffening, strengthening and toughening mechanisms in natural materials. In particular, the following conclusions can be drawn:

(1) The end-concentrated interface design exhibits excellent effective interface shear stiffness and strength, and the center-concentrated design is excellent in the effective shear strength, failure strain, and work of fracture. Both of them are significantly superior to the uniform design. This provides an explanation why the end-concentrated and center-concentrated distributions of interfacial bridges/crosslinks are widely seen in natural biological materials.

(2) The ratio of effective working crosslinks is defined to quantitatively measure the utilization efficacy of the crosslinks. The concept can be generalized to any interfacial materials. Our study shows that the end-concentrated and center-concentrated interface designs can yield a distinctly higher efficacy of crosslink utilization.

(3) A set of analytical formulae are derived, expressing the effective shear modulus, shear strength, and failure initiation shear strain as functions of a variety of geometrical and physical parameters for the three typical interface designs. These formulae can be

used to predict the mechanical properties of different interface designs as well as to figure out the optimal design through tuning a range of geometrical and physical parameters.

CRediT authorship contribution statement

Kun Geng: Conceptualization, Methodology, Software, Validation, Writing - original draft. **Wen Xie:** Methodology. **Bin Chen:** Validation. **Qifang Yin:** Validation. **Yanan Yuan:** Conceptualization. **Zuoqi Zhang:** Conceptualization, Methodology, Supervision, Writing - review & editing.

Declaration of Competing Interest

The authors declare that they have no known competing financial interests or personal relationships that could have appeared to influence the work reported in this paper.

Acknowledgements

The work was supported by National Natural Science Foundation of China (Grant Nos. 11772240, 11720101002, 11542001, 11502175), Jiangsu Natural Science Foundation (Grant No. BK20150381), the Fundamental Research Funds for the Central University and the Innovative Group Development Program at School of Civil Engineering, Wuhan University.

Data availability

The raw/processed data required to reproduce these findings cannot be shared at this time as the data also forms part of an ongoing study.

References

[1] Menig R, Meyers MH, Meyers MA, Vecchio KS. Quasi-static and dynamic mechanical response of Haliotis rufescens (abalone) shells. Acta Mater 2000;48(9):2383–98.
[2] Jackson AP, Vincent JFV, Turner RM. The mechanical design of nacre. Proc R Soc Lon 1988;234(1277):415–40.
[3] Kamat S, Su X, Ballarini R, Heuer AH. Structural basis for the fracture toughness of the shell of the conch Strombus gigas. Nature 2000;405(6790):1036–40.
[4] Mayer G. Rigid biological systems as models for synthetic composites. Science 2005;310(5751):1144–7.
[5] Mayer G, Sarikaya M. Rigid biological composite materials: Structural examples for biomimetic design. Exp Mech 2002;42(4):395–403.
[6] Launey ME, Ritchie RO. On the fracture toughness of advanced materials. Adv Mater 2010;21(21):2103–10.
[7] Sarikaya M, Gunnison KE, Yasrebi M, Aksay IA. Mechanical property-microstructural relationships in abalone. Shell. Mrs Proceedings. 1989;174.
[8] Addadi L, Weiner S. Biomineralization – A pavement of pearl. Nature 1997;389(6654):912–4.
[9] Schaffer TE, Ionescu-Zanetti C, Proksch R, Fritz M, Walters DA, Almqvist N, et al. Does abalone nacre form heteroepitaxial nucleation or by growth through mineral bridges? (vol 9, pg 1731, 1997). Chem Mater 1998;10(3):946.
[10] Buehler MJ, Yung YC. Deformation and failure of protein materials in physiologically extreme conditions and disease. Nat Mater 2009;8(3):175–88.
[11] Zhang Z, Zhang Y-W, Gao H. On optimal hierarchy of load-bearing biological materials. Proc. R. Soc. B 2011;278(1705):519–25. https://doi.org/10.1098/rspb.2010.1093.
[12] Chen B, Wu PD, Gao H. A characteristic length for stress transfer in the nanostructure of biological composites. Compos Sci Technol 2009;69(7–8):1160–4.
[13] Lei HJ, Zhang ZQ, Han F, Liu B, Zhang YW, Gao HJ. Elastic bounds of bioinspired nanocomposites. J Appl Mech Trans ASME 2013;80(6).
[14] Lei HF, Zhang ZQ, Liu B. Effect of fiber arrangement on mechanical properties of short fiber reinforced composites. Compos Sci Technol 2012;72(4):506–14.
[15] Zhang ZQ, Liu B, Huang Y, Hwang KC, Gao H. Mechanical properties of unidirectional nanocomposites with non-uniformly or randomly staggered platelet distribution. J Mech Phys Solids 2010;58(10):1646–60.
[16] Ji B, Gao H. Mechanical properties of nanostructure of biological materials. J Mech Phys Solids 2004;52(9):1963–90.
[17] Kotha SP, Li Y, Guzelsu N. Micromechanical model of nacre tested in tension. J Mater Sci 2001;36(8):2001–7.
[18] Zuo S, Wei Y. Effective elastic modulus of bone-like hierarchical materials. Acta Mech Solida Sin 2007;20(3):198–205.
[19] Zhang P, To AC. Highly enhanced damping figure of merit in biomimetic hierarchical staggered composites. J Appl Mech Trans ASME 2014;81(5).
[20] Liu L, Jiang Y, Boyce M, Ortiz C, Baur J, Song J, et al. The effects of morphological irregularity on the mechanical behavior of interdigitated biological sutures under tension. J Biomech 2017;58:71–8.
[21] Gao C, Li Y. Mechanical model of bio-inspired composites with sutural tessellation. J Mech Phys Solids 2019;122:190–204.
[22] Begley MR, Philips NR, Compton BG, Wilbrink DV, Ritchie RO, Utz M. Micromechanical models to guide the development of synthetic 'brick and mortar' composites. J Mech Phys Solids 2012;60(8):1545–60.
[23] Rabiei R, Bekah S, Barthelat F. Failure mode transition in nacre and bone-like materials. Acta Biomater 2010;6(10):4081–9.
[24] Lin A-Y-M, Meyers MA. Interfacial shear strength in abalone nacre. J Mech Behav Biomed Mater 2009;2(6):607–12.
[25] Song F, Soh AK, Bai YL. Structural and mechanical properties of the organic matrix layers of nacre. Biomaterials 2003;24(20):3623–31.
[26] Meyers MA, Lin A-Y-M, Chen P-Y, Muyco J. Mechanical strength of abalone nacre: Role of the soft organic layer. J Mech Behav Biomed Mater 2008;1(1):76–85.
[27] Alghamdi S, Tan T, Hale-Sills C, Vilmont F, Xia T, Yang J, et al. Catastrophic failure of nacre under pure shear stresses of torsion. Sci Rep 2017;7(1):1–7.
[28] Alghamdi S, Du F, Yang J, Tan T. The role of water in the initial sliding of nacreous tablets: Findings from the torsional fracture of dry and hydrated nacre. J Mech Behav Biomed Mater 2018;88:322–9.
[29] Gu GX, Libonati F, Wettermark SD, Buehler MJ. Printing nature: Unraveling the role of nacre's mineral bridges. J Mech Behav Biomed Mater 2017;76:135–44.
[30] Niebel TP, Bouville F, Kokkinis D, Studart AR. Role of the polymer phase in the mechanics of nacre-like composites. J Mech Phys Solids 2016;96:133–46.
[31] Espinosa HD, Rim JE, Barthelat F, Buehler MJ. Merger of structure and material in nacre and bone – Perspectives on de novo biomimetic materials. Prog Mater Sci 2009;54(8):1059–100.
[32] Wegst UGK, Bai H, Saiz E, Tomsia AP, Ritchie RO. Bioinspired structural materials. Nat Mater 2015;14(1):23–36.
[33] Xin Z, Zhang X, Duan Y, Xu W. Nacre-inspired design of CFRP composite for improved energy absorption properties. Compos Struct 2018;184:102–9.
[34] Ryu S, Lee Y, Hwang J-W, Hong S, Kim C, Park TG, et al. High-strength carbon nanotube fibers fabricated by infiltration and curing of mussel-inspired catecholamine polymer. Adv Mater 2011;23(17):1971–5.
[35] Zhang Z, Liu B, Zhang Y-W, Hwang K-C, Gao H. Ultra-strong collagen-mimic carbon nanotube bundles. Carbon 2014;77:1040–53.
[36] Lin M, Sun XY, Xie W, Zhang ZQ. Load-transfer and failure behaviors of crosslinked interfaces in collagen-mimic carbon nanotube bundles. Int J Mech Sci 2018;135:376–82.
[37] Sun XY, Zhang ZQ, Xu YJ, Zhang YW. An elastic model for bioinspired design of carbon nanotube bundles. Acta Mech Sin 2015;31(2):205–15.
[38] Park O-K, Choi H, Jeong H, Jung Y, Yu J, Lee JK, et al. High-modulus and strength carbon nanotube fibers using molecular cross-linking. Carbon 2017;118:413–21.
[39] Rahman MM, Zainuddin S, Hosur MV, Robertson CJ, Kumar A, Trovillion J, et al. Effect of NH2-MWCNTs on crosslink density of epoxy matrix and ILSS properties of e-glass/epoxy composites. Compos Struct 2013;95:213–21.
[40] Xie W, Yuan Y, Zhang Z. A floquet-based bar-spring model for the dynamic modulus of bioinspired composites with arbitrary staggered architectures. J Appl Mech 2019;86(9):091007.